Journal of
Materials Chemistry A

ROYAL SOCIETY
OF CHEMISTRY

PAPER

View Article Online
View Journal | View Issue

Check for updates

Cite this: *J. Mater. Chem. A*, 2025, **13**, 24619

Structural origin of disorder-induced ion conduction in $NaFePO_4$ cathode materials†

Rasmus Christensen, [a] Kristin A. Persson [bc] and Morten M. Smedskjaer [*a]

Received 20th March 2025
Accepted 30th June 2025

DOI: 10.1039/d5ta02295a

rsc.li/materials-a

Most modern battery technologies depend on solid-state crystalline cathode materials. However, some of these materials are constrained by the low ionic conductivity of their most stable phases. An example of this is maricite ($NaFePO_4$). Interestingly, experiments have shown that maricite can improve its rate capability through disordering (amorphization). However, experimental characterization of amorphous cathode materials remains a major challenge, hindering a clear understanding of the structural origin of the disorder-induced improvement in sodium-ion mobility. To address this, we here employ molecular dynamics simulations by first training a machine learning potential for $NaFePO_4$ based on the atomic cluster expansion approach and a batch active learning potential parameterization scheme. This potential is then applied to explore the structural and dynamical properties of $NaFePO_4$ glasses as cathode materials. Specifically, we investigate the effect of glass structure on sodium-ion diffusion, revealing the relative influences of short-range and medium-range order features. We find significant heterogeneity in sodium-ion diffusivity in the glass, with fast-conducting ions residing in less constrained atomic environments with fewer P and Fe neighbors. These more mobile ions are also surrounded by larger ring-type structures. Overall, the results and developed approach present promising avenues for developing high-performance glassy cathodes for next-generation batteries.

1. Introduction

The rapid electrification of many sectors of society has created a growing need for new battery technologies with improved performance, lifetime, and safety.[1–3] Current Li-ion and future Li-metal batteries face limitations in terms of their cost and sustainability, due to the limited natural availability of lithium for electrode and electrolyte materials and commonly used transition metals (*e.g.*, cobalt) for the cathode.[4,5] As such, developing low-cost and sustainable battery materials based on abundant resources is highly desired.[6] To this end, sodium-based compounds have emerged as promising candidates to address some of these challenges, due to the large abundance and low cost of sodium.[6] Although the gravimetric and volumetric energy densities of Na-ion batteries cannot exceed those of the Li analogs due to the larger size and lower reducing potential of Na, such batteries can still be highly valuable for large-scale electrical storage where energy density is not a critical issue.[7]

To realize large-scale Na-ion batteries, new cathode materials are needed. Several candidates have been proposed, including transition metal oxides like $NaMnO_2$,[8,9] and polyanionic compounds, typically based on one or more transition metals and a polyanion group such as $(PO_4)^{3-}$, $(SiO_4)^{4-}$, or $(SO_4)^{2-}$.[10] One system of particular interest is $NaFePO_4$, as it offers a highly abundant and environmentally friendly combination of elements.[11] The Li-containing analog, $LiFePO_4$, in the olivine crystal structure, is a known high-performance commercial cathode material, which exhibits a reversible capacity of about 160 mA h g^{-1} and a working voltage close to 3.5 V *vs.* Li/Li^+.[12] However, contrary to $LiFePO_4$, the most thermodynamically stable crystal phase of $NaFePO_4$, maricite, is electrically inert since the Na atoms are trapped in their local atomic environments in the crystal structure.[11] This limitation necessitates the exploration of methods to enhance the conductivity and electrochemical performance of $NaFePO_4$.[11,13,14]

One of the approaches to increase the conductivity includes the formation of olivine $NaFePO_4$ through delithiation of $LiFePO_4$ followed by sodiation, giving rise to a specific capacity of about 110 mA h g^{-1} with a discharge voltage of about 2.8 V.[15] An alternative approach focuses on disordering maricite. Kim *et al.*[16] reported that maricite $NaFePO_4$ could be transformed into an amorphous phase during the first charging at 4.5 V for 5 h. Interestingly, the amorphous $NaFePO_4$ phase showed a reversible capacity of about 142 mA h g^{-1} (92% of the theoretical value) at 0.05C during the first cycle and outstanding

---

[a] *Department of Chemistry and Bioscience, Aalborg University, Denmark. E-mail: mos@bio.aau.dk*

[b] *Department of Materials Science and Engineering, University of California, Berkeley, CA, USA*

[c] *Materials Science Division, Lawrence Berkeley National Laboratory, CA, USA*

† Electronic supplementary information (ESI) available. See DOI: https://doi.org/10.1039/d5ta02295a

cyclability (95% retention after 200 cycles). This discovery sparked great interest in exploring various methods for obtaining both partially and fully amorphous $NaFePO_4$, such as high-potential charging,[17] high-energy ball milling,[13,14,18] melt quenching[19] and laser irradiation,[20] all exhibiting improved electrochemical activity compared to maricite $NaFePO_4$. Notably, disorder can also be used to improve the ion conductivity in solid electrolyte materials for batteries.[21]

Understanding the interplay between structural disorder and sodium-ion mobility is crucial for optimizing these cathode materials for practical use. Previous work[14,22] has found that a shift in Fe local structure from edge-sharing FeO_6 octahedra to FeO_n polyhedral upon amorphization is a key factor for the enhanced electrochemical performance.[14] However, further investigations are needed to understand the detailed structural origins and to identify the optimal conditions for achieving improved ion dynamics. To investigate how disorder affects the ion dynamics in $NaFePO_4$, we here rely on molecular dynamics (MD) simulations. Ideally *ab initio* MD based on density functional theory (DFT) would be performed to study the amorphous structure and ion dynamics of $NaFePO_4$ with high accuracy. However, due to simulation length and time scales associated with accurately capturing these properties in amorphous materials, relying solely on *ab initio* MD is currently intractable due to the computational cost. Hence, to simulate these systems, we use more computationally efficient methods. To this end, classical interatomic potentials exist, such as the Teter potential,[23] which has been extended to include parameters for sodium iron phosphates[24–26] (hereafter simply referred to as the Teter potential), and the BMP potential.[27,28] However, we here focus on machine learning interatomic potentials (MLIPs) due to their promised balance of both high accuracy and computational efficiency, but to our knowledge, no MLIP for amorphous $NaFePO_4$ currently exists. We note that several "universal" MLIPs have been proposed in recent years,[29,30] but these potentials have shown difficulties when modelling non-equilibrium and high-temperature structures, questioning their suitability for simulating amorphous and melt-quenched glass materials.[31,32]

In this work, we parameterize a new MLIP for $NaFePO_4$ by employing the atomic cluster expansion (ACE)[33,34] as the MLIP architecture, as it offers an efficient way to model complex systems. As stated, many current attempts to apply MLIP to amorphous systems suffer from pitfalls such as high temperature instability, especially when simulating structures outside the distribution of the training data.[35] Furthermore, common approaches for obtaining training data for these MLIPs involve sampling structures at various timesteps from long AIMD trajectories to construct datasets.[36] This process can be a very computationally costly procedure, while still not guaranteeing a good coverage of the structural feature space. To address these issues, we here propose a new potential parameterization scheme based on batch active learning,[37] to iteratively improve the potential by using the potential itself to sample structures, which are significantly different from what is already included in the training data. We believe the proposed parameterization workflow is generally applicable to generate MLIPs for amorphous and other disordered materials. Building on the new MLIP and the Teter and BMP classical potentials, we perform MD simulations to obtain amorphous $NaFePO_4$ structures, from which ion dynamics are sampled. These simulations allow us to explore the effects of disorder on ionic transport, providing structural insights to guide the rational design of next-generation solid electrodes.

2. Methods

2.1 Computational details

All DFT calculations were conducted in VASP software[38–40] using the projector augmented-wave method.[41] The GGA-PBE functional[42] was used with a kinetic energy cutoff of 520 eV and 1 × 1 × 1 gamma point sampling. DFT + U was used for the evaluation of Fe ion, with U set to 5.1 eV and J to 0 eV. This was done to ensure consistency with the materials project dataset.[43] The convergence criterion for DFT simulations was 10^{-5} eV per atom unless otherwise specified. MD simulations using classical potentials and the trained ACE MLIPs were performed in LAMMPS[44] compiled with the ML-PACE package[34] and performed on NVIDIA V100 GPUs using KOKKOS. For simulations in the NVT ensemble, a Nosé–Hoover thermostat with temperature damping constant of 100 fs was applied, while for NPT simulations, we added a Nosé–Hoover barostat with a pressure damping constant of 1000 fs.

2.2 Potential parametrization workflow

To parameterize the MLIP for $NaFePO_4$, we applied the workflow outlined in Fig. 1A. Each step in the workflow is explained in detail in the following sections. The workflow frameworks for structure generation, model training, and evaluation are based on several open-source python packages, such as ASE,[45] pymatgen,[46] Atomate2 (ref. 47), Jobflow,[48] Fireworks[49] and PACEMAKER,[33,34,37,50] and can be found at Github: **https://github.com/R-Chr/vitrum**. The proposed framework facilitates parameterization of machine learning potentials using ACE for amorphous materials, enabling semi-automated generation of such potentials for given amorphous systems of interest. To ensure the high-temperature stability of the resulting potential, the workflow is based on initially generating and learning from short high-temperature DFT simulations of strained pseudo-random structures, and subsequently improving on this using batch active learning.

2.2.1 Random structure generation. Although we are here mainly interested the properties of the $NaFePO_4$ system, we sample a much broader composition space during the training of our model. That is, within the ternary composition diagram of $NaO_{0.5}$, $PO_{2.5}$ and FeO oxides, we sample the entire ternary diagram in 10 mol% increments as shown in Fig. 1B. This is done to increase the transferability of the potential to other compositions in the future, but also to ensure that the model is exposed to many different chemical environments that may influence the performance and stability when simulating $NaFePO_4$ systems. For each chosen composition, an initial pseudo-random atomic structure of ∼100 atoms was generated

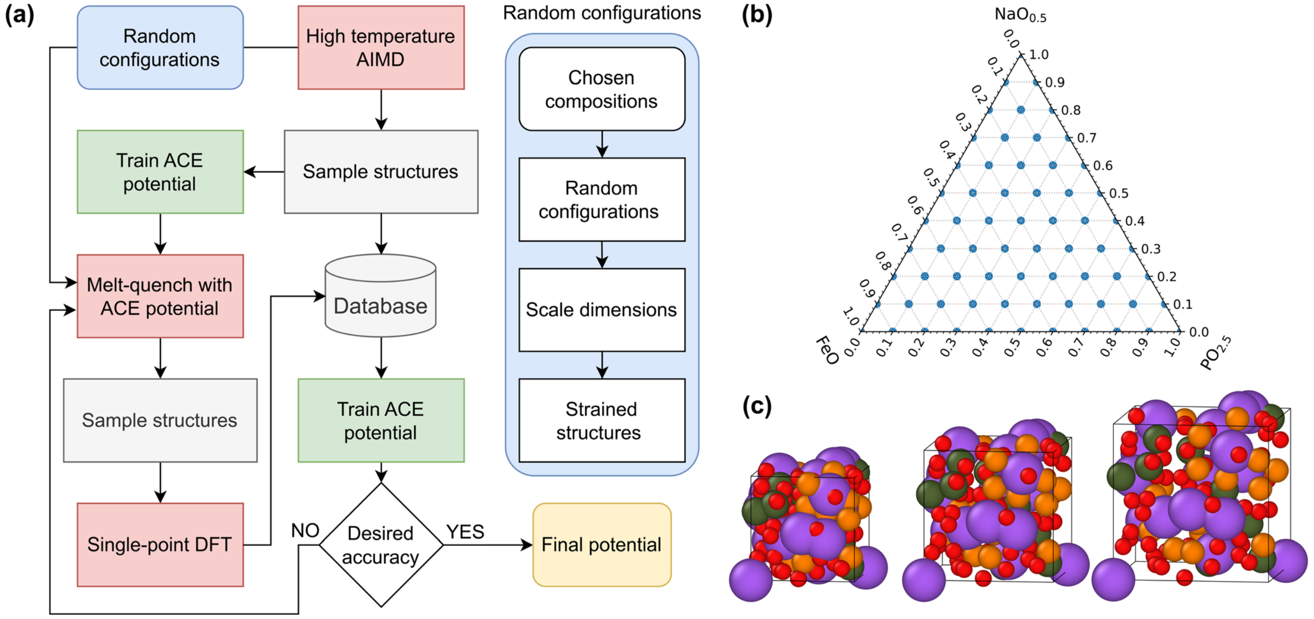

Fig. 1 (a) Flow diagram of the ACE potential parameterization workflow. (b) Ternary diagram of studied sodium iron phosphate compositions used for training the ACE potential. (c) Pseudo-random atomic structures of Na_2O–FeO–P_2O_5 generated based an initial estimated density and subsequent scaling of side lengths by 0.8 (left), 1.0 (middle), and 1.2 (right).

by randomly placing atoms in the simulation box while ensuring a minimum interatomic distance of 1.7 Å to avoid unrealistic overlaps. The initial density of a given composition was chosen by matching it to the average density of its corresponding crystal phase as available in the materials project database.[43] If no precise compositional match was available in the database, the density was chosen as the average density of all crystals in the database, containing exactly the same atom types as the given composition. This approach allowed for a reasonable and consistent initial density guess for amorphous systems where the real density is unknown. The initial structure was subsequently rescaled in all directions, either stretched or compressed by 20%, producing three random structures for each composition to increase the types of chemical environments sampled throughout training (Fig. 1C). In the present study, all compositions are balanced to considered only a single oxidation state of each species: +1 for Na, +2 for Fe, +5 for P and −2 for O (see Discussion on the choice of iron redox state in Section 3.5).

2.2.2 Initial high temperature dataset. An initial high temperature dataset was generated using AIMD by sampling structures from 200 fs trajectories at 5000 K of the generated random structures in the NVT ensemble using a 2 fs timestep. From these short trajectories, structures were sampled every 40 fs. These high temperature trajectories explored the initial relaxation of the random systems, and hence sampled a wide range of configurations, ensuring that the dataset captured a diverse set of structural features and potential energies and forces. The energies and forces of the sampled configuration were collected to form the initial dataset of 980 structures used for training the initial ACE potential.

2.2.3 Machine learning interatomic potential fitting. The chosen MLIP architecture, ACE, is used to learn and predict the energies and forces of the given atomic structures. We use the ACE methodology as implemented in the PACEMAKER software.[33,34,37,50] A detailed walkthrough of the principles of ACE is provided elsewhere.[33] To construct an ACE potential, the atomic environments were described using spherical harmonics, up to an angular momentum $l_{\max}$ and radial basis functions represented by Bessel functions. The atomic interactions were evaluated up to a limit of 6.5 Å, at which point the radial components approached zero. For the ACE model embedding, we used a complex type embedding (eqn (1)), as previously proposed by Erhard *et al.*,[51] who showed this type of embedding to be optimal for parameterizing a MLIP for amorphous SiO_2.

$$E_i = \phi + \sqrt{\phi} + \sum_i \phi^{f_i}, \quad f_i \in \left\{\frac{1}{8}, \frac{1}{4}, \frac{3}{8}, \frac{3}{4}, \frac{7}{8}, 2\right\} \tag{1}$$

In eqn (1), the energy of atom i E_i is calculated from expansion of the atomic properties ϕ_i. For ϕ_i we used 248 basis functions per atom type, totalling 992 basis functions and 8692 parameters. For the radial basis functions, we used Bessel functions. For the potential optimization, the loss function of eqn (2) was used, giving the squared deviation in predicted energy Δ_E^2 and forces Δ_F^2, with a weighting ratio between force and energy deviation κ of 0.01.

$$\wedge = (1-\kappa)\Delta_E^2 + \kappa\Delta_F^2) \tag{2}$$

We utilized the BFGS algorithm for optimization with a maximum number of iterations of 2000, and an early stopping criterion with a patience of 150 iterations for the minimum relative training and test loss per iteration of 5×10^{-4} and $1 \times$

10^{-4}, respectively. The potentials were optimized in a ladder scheme, with batches of 160 basis functions being added to the potential at a time, and trained until the training stopping criterion before adding the next batch. We note that the BFGS algorithm was applied as it is one of the currently supported algorithms in the PACEMAKER framework. However, if supported in the future, the use of more sophisticated optimization methods, such as Bayesian optimization, could potentially be beneficial for better navigating high-dimensional search spaces.

2.2.4 Batch active learning. To iteratively improve the trained MLIP, we used the potential to generate the new structures, for which the potential had a high uncertainty. Several methods exist for calculating the uncertainty of MLIP predictions, such as Ensemble uncertainty,[52,53] Bayesian estimation,[54,55] and the D-optimality criterion using the MaxVol algorithm.[37,56,57] We here choose to use the D-optimality method due to its low computational overhead, and its implementation in the PACEMAKER optimization framework.[37] This uncertainty algorithm offers an assessment of the extent to which a particular structure resembles other structures present in the training set through a metric referred to as the extrapolation grade. The approach allowed us to prioritize structures that were likely to yield new insights, thereby enhancing the efficiency of our exploration in the vast configurational space of amorphous materials.

In many active learning procedures, such as on-the-fly learning,[55] sampling of a structure, evaluation with DFT and retraining the model are done in serial, *i.e.*, the model is updated after every new sampled structure. However, due to the non-negligible computational time required to evaluate structures and retrain the potential, we opted for a batch approach to facilitate parallel sampling and evaluation of multiple structures. In this way, more new information could be included in each retraining of the potential.

To sample structures with high uncertainty, while also generating predictions of the equilibrium liquid and glass structures, we conducted melt-quench MD simulations using the parameterized potential. Starting from new random structures, *i.e.*, same compositions and deformations as the high temperature dataset but rerandomized, we relaxed the structures at 5000 K in the NVT ensemble for 10 ps. This was followed by a gradual cooling process to 0 K with a cooling rate of 10 K ps^{-1}, sampling structures at every 1000 K interval. This approach allows for the rapid generation of new proposed liquid and glass structures by the model. During these simulations, we also tracked the value of the extrapolation grade of each atom from the D-optimitality method. This was done to identify uncertain structures in its prediction, *i.e.*, structures with atoms showing an extrapolation grade above 2.5. All such structures were sampled for later evaluation. Any simulation showing atoms with an extrapolation grade above 30 was terminated early, as they were deemed too unstable. Simulations which ended before being completed were not restarted. After attempting to perform all the simulated melt-quenches, the structures sampled in the batch due to a high extrapolation grade were collected and evaluated for redundancies, *i.e.*, to check if similar uncertain structures showed up several times in the sampled structures. This was done by evaluating all structures sampled due to a high extrapolating grade, choosing the optimal subset of them by again using the D-optimality criterion. Here, we selected up to 500 structures with the highest extrapolation grades when compared to each other. This evaluation helped to keep the dataset manageable, ensuring that mainly unique and potentially valuable structures were retained for further analysis. Subsequently, these selected structures were evaluated with single point DFT calculation to obtain their energy and forces and appended to the existing dataset. During the parameterization of the $\mathrm{NaFePO_4}$ potential, this process was repeated three times, producing a final dataset of 4344 structures.

2.3 $\mathrm{NaFePO_4}$ glass structure generation

Using the final ACE MLIP and the two existing BMP and Teter classical interatomic potentials, we generated glass structures of $\mathrm{NaFePO_4}$ by simulated melt-quench simulation (Fig. 2A). Potential parameters for the classical potentials are given in ESI, Tables S1–S5.† We started from a pseudo-random structure of 3003 atoms generated to have a density of 3.38 g cm^{-3}, corresponding to the extrapolated density of $\mathrm{NaFePO_4}$ glass based on previous experimental results for $\mathrm{NaFePO_4}$ systems with varying composition and crystallinity.[19]

An overview of the simulation procedures is shown on Fig. 2B. We started by performing an energy minimization of the random structure, followed by a 20 ps initialization of the system at 300 K, with the first 10 ps in the NVT ensemble, followed by 10 ps in the NPT ensemble at zero external pressure. The system was then instantaneously raised to 3000 K and relaxed for a total of 200 ps (100 ps in the NVT ensemble, followed by 100 ps in the NPT ensemble) at zero external pressure. Following this equilibration procedure, the systems were subjected to gradual cooling to 300 K with a cooling rate of 1 K ps^{-1} (NPT, zero external pressure), whereafter the system was relaxed for a 100 ps at 300 K (NPT, zero external pressure) to obtain relaxed glass structures.

From these structures, we sampled the diffusion properties at varying temperatures (500, 700, 900, 1100, 1300, and 1500 K). To sample diffusion at elevated temperatures, the glass structure was gradually heated to the target temperature with a heating rate of 1 K ps^{-1}, and then it was equilibrated for 100 ps at the target temperature, before the diffusion was measured for 10 ns. To investigate the effect of density changes and pressure build up (during heating to the target temperature of the diffusion simulations), two sets of diffusion simulations were conducted for each temperature, where heating was conducted in the NVT and NPT ensembles, respectively. The entire diffusion sampling was conducted in the NVT ensemble to ensure the structure maintained a consistent density, and that the diffusion was sampled at the target temperature. Five glass structures were prepared and evaluated for each studied potential, replicating the same simulation workflow.

2.3.1 DFT reference glass structure. To compare the performance of the MLIP in reproducing the glass structure of $\mathrm{NaFePO_4}$, we produced three $\mathrm{NaFePO_4}$ glasses from AIMD

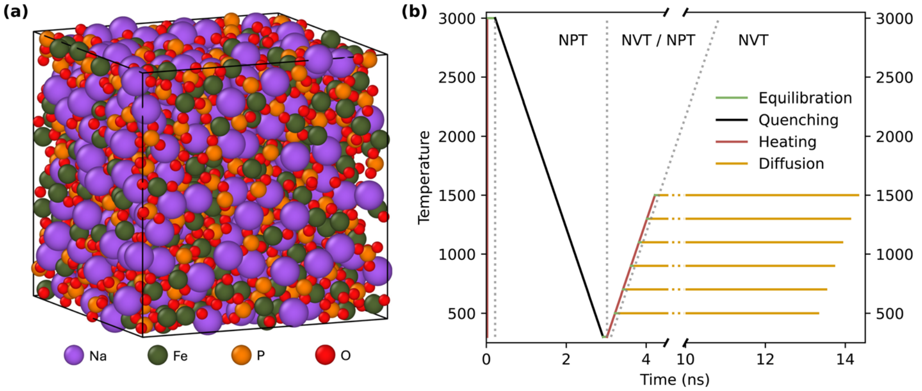

Fig. 2 (a) Atomic structure of simulated $NaFePO_4$ glass with the ACE machine learning potential. (b) Overview of melt-quenching and diffusion simulation procedures.

simulations using DFT. The initial structures for the DFT calculations were generated from melt-quench simulations of 245 atoms with the BMP potential, using the same cooling scheme described above. We started from the BMP generated glass structure to ensure we started from a stable structure, improving the energy convergence during the self-consistent field calculations, while still ensuring that the final glass structure from DFT was not biased by a possible retention of the glass structure of the ACE potential. The initial structure was first geometry optimized, and subsequently equilibrated at 3000 K for 2 ps. This was followed by quenching the structures to 300 K with a rate of 100 K ps^{-1}, and subsequent equilibration at 300 K for 1 ps. All the simulation steps were performed in the NVT ensemble. A larger convergence criterion for DFT simulations of 5×10^{-5} eV per atom was applied for these simulations to ensure computational efficiency.

2.3.2 Elastic properties. Elastic properties of the glass structures produced with the interatomic potentials and DFT were calculated. Glass structures from the interatomic potentials were subjected to 20 stepwise elongations and compressions of $\varepsilon = 0.0001 = 0.01\%$ in the tensile directions *xx*, *yy*, and *zz* as well as in the shear directions *xy*, *xz*, and *zy* under the assumption of isotropic structures. Structures from DFT were subjected to single step deformation in each direction of $\varepsilon = 0.005 = 0.5\%$. After each deformation step, the structures were energy minimized, before measuring stress. From the resulting stress–strain curves, the elastic constants were obtained by linear regression, with C_{11}, C_{12}, and C_{44} being calculated as averages from the elastic tensor under the assumption of isotropy. This enabled a calculation of the elastic moduli and Poisson's ratio (ν) as follows:

$$E = \frac{(C_{11} - C_{12})(C_{11} + 2 \times C_{12})}{C_{11} + C_{12}} \quad (3)$$

$$G = \frac{C_{11} - C_{12}}{2} \quad (4)$$

$$K = \frac{C_{11} + 2 \times C_{12}}{3} \quad (5)$$

$$G = \frac{C_{12}}{C_{11} + C_{12}} \quad (6)$$

3. Results and discussion

3.1 ACE potential training

To evaluate the performance of the developed ACE MLIP, we first evaluate the final energy and force prediction errors of the final training and test datasets. Fig. 3 shows parity plots of the predicted *versus* reference energy (Fig. 3A) and forces (Fig. 3B). The final obtained mean average errors for the training and test set for energies were 26.66 and 26.38 meV per atom, respectively, while for the force components they were 499.22 and 515.59 meV Å^{-1}, respectively. We note that although these errors are relatively large compared to errors usually obtained for MLIPs,[35,51] the present data set contains many high-energy configurations as reflected from the large span of energies and forces seen in Fig. 3. Hence, the obtained errors suggest that an accurate potential for investigating glass structure and dynamics has been obtained. Further, we note that while low energies and forces errors are very desirable when training an MLIP, several other criteria are also important, such as stability, computational efficiency, and ability to replicate the structural and physical properties of materials. This will be discussed in the following.

The high temperature stability of the potential is important as it allows for obtaining glass structures through simulated melt-quench simulations. As seen in ESI, Fig. S1,† a high temperature stability test of the initial and final ACE potential was performed on a pseudo random structure of 3003 atoms of $NaFePO_4$ simulated at 5000 K for 10 ps in the NVT ensemble at zero pressure. We find that while the initial ACE potential before active learning is trained purely on structures sampled from the high temperature AIMD simulations, the potential quickly (after only 11 fs) experiences high energy and force errors, causing the velocity of the atoms to quickly increase and ultimately terminate the simulation. On the contrary, the final ACE potential after active learning does not exhibit any sudden

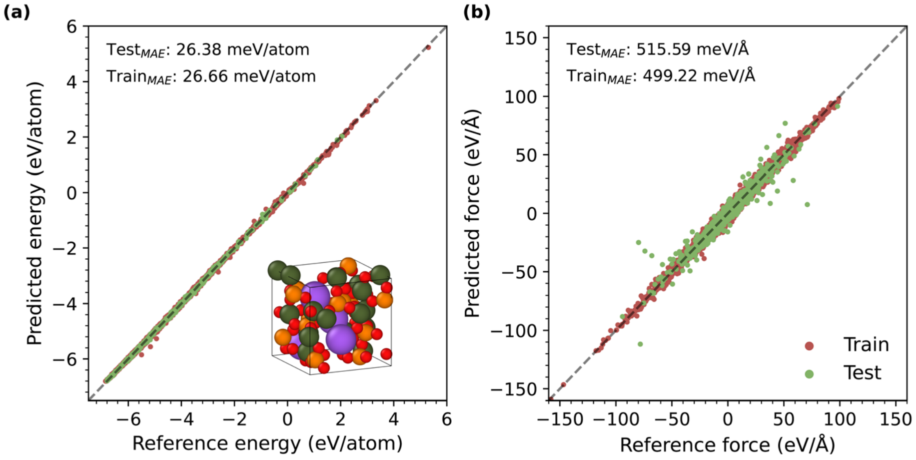

Fig. 3 Parity plots for (a) energy and (b) force components of the ACE potential for the training (red) and test (green) datasets. The mean average errors, MAE, for each of the datasets is reported on the figures. An example atomic structure included in the dataset is shown in panel (a).

increases in the energy and forces, validating the present approach to increase the high temperature stability of the potential. Furthermore, throughout the use of the final potential, we did not encounter any issues related to its high temperature stability.

While a comprehensive analysis of the computational efficiency of the of the new ACE potential has not been performed, we find that on NVIDIA V100 GPU, we can simulate at 0.07–0.1 timesteps per s per atom, *i.e.*, a performance very comparable to that of the classical potentials used herein when run on the same hardware. This efficiency agrees well with previous reports of the computational efficiency of the ACE method.[34] As such, the high computational efficiency of our MLIP allows us to simulate the dynamics of the $NaFePO_4$ glass systems at relatively long time scales $>10^5$ fs.

3.2 Structural characterization

We compare the structural features of the simulated $NaFePO_4$ glasses generated using the ACE MLIP to those of the BMP and Teter classical interatomic potentials as well as independent AIMD simulations conducted separately from the training of the ACE potential. We note that while these DFT simulations are expected to give the best description of the glass structure due to the higher accuracy of DFT, they are limited by the high cooling rate (100 *vs.* 1 K ps^{-1} for MLIP) and small system size (245 *vs.* 3003 atoms for MLIP) due to the computational cost. Consequently, the glass structures generated using AIMD are expected to be more disordered than what would be obtained using a lower cooling rate and have limited information regarding medium-range order structures. Therefore, while we compare the results of ACE and classical potentials to those based on DFT, perfect agreement should not be expected due to the difference in preparation conditions.

The density of glasses produced using the MLIP and classical potentials is compared in Table 1, showing similar simulated densities around 3.0 g cm^{-3}. This is lower than the extrapolated experimental density of (crystal-free) amorphous $NaFePO_4$,[19] which is likely caused by several factors, such as (i) the high cooling rate used in simulations, leading to a higher fictive temperature and hence lower density, and (ii) the lack of any corrections for dispersive Van der Walls interactions for the used PBE functional, which can lead to an underestimation of the cohesive interactions in materials, leading to a decrease in the density.[58,59]

In addition to density, we have evaluated the elastic properties of the $NaFePO_4$ glass structures. Specifically, we computed Young's modulus, shear modulus, bulk modulus, and Poisson's ratio of the glass structures from DFT and compared them with results from the ACE, BMP, and Teter potentials (see ESI, Table S6†). These comparisons reveal that all three potentials reasonably reproduce the DFT-computed elastic properties, with the BMP potential yielding the closest match across all metrics.

In all the simulated glass structures, P exhibits its expected coordination number of 4, while the average coordination number of Fe varies between the different simulation methods, ranging from 4.46 to 5.15 (Table 1). We here observe good agreement between the structures generated using ACE MLIP and DFT, both giving a Fe coordination number above 5.1. Based on the number of P–O–P and P–O–Fe bonds per P atom in Table 1, we conclude that an avoidance of interlinking phosphates is featured in all simulated glass structures. Isolated phosphate tetrahedra are the primary phosphate structure, dispersed between Fe ions.

Fig. 4 shows the partial oxygen radial distribution functions $g_{ij}(r)$ (Fig. 4A), total structure factor $S(Q)$ (Fig. 4B) and selected bond angle distributions (Fig. 4C). The remaining radial distribution functions are shown in ESI, Fig. S2.† The radial distribution functions reveal that the ACE-based potential accurately reproduces the short-range order structures predicted by DFT calculations. Specifically, the ACE potential shows improved accuracy in P–O and O–O bond lengths and peak intensities compared to both the Teter and BMP potentials. However, a notable exception is the Fe–O bond, where the ACE potential overestimates the peak intensity and shifts the

Table 1 Structural properties of simulated $NaFePO_4$ glass, including density, T_g, average P and Fe coordination number, and number of P–O–P and P–O–Fe bonds per P atom. For T_g, the first reported number is based on simulations in NVT, while the number in parentheses is from NPT. *Density of the DFT glass structures is not reported as it remains unchanged from the starting structure generated with the BMP potential due to quenching in the NVT ensemble

Simulation method	Density (g cm^{-3})	T_g (K)	Average P coordination	Average Fe coordination	P–O–P bonds per P atom	P–O–Fe bonds per P atom
ACE MLIP	3.071	762 (740)	4.00	5.15	0.08	3.53
Teter	2.985	1045 (985)	4.00	4.70	0.12	3.29
BMP	3.017	999 (898)	4.00	4.46	0.04	3.39
DFT	N/A*	—	4.00	5.11	0.05	3.43

bond length to shorter distances. To examine the medium-range order of the glasses, we consider the calculated structure factor (Fig. 4B). While the ACE MLIP shows excellent agreement with the result of DFT based simulations at high Q, significant discrepancies emerge at lower Q. However, the limited system size of AIMD simulations, makes the low Q structure factor calculations inherently unreliable. As such, to properly assess the predicted structure factors, experimental neutron or X-ray total scattering data would be needed. To the authors' knowledge, such data has not been reported yet for $NaFePO_4$ glass. Instead, we have computed glass structures of related compositions, where experimental total scattering data is available. This includes P_2O_5, $20Na_2O$–$80P_2O_5$, $50Na_2O$–$50P_2O_5$, $40FeO$–$60P_2O_5$, and $50FeO$–$50P_2O_5$ glasses. As seen in the ESI, Fig. S3,† the glass structures, as quantified by the structure factor $S(Q)$, produced with the ACE potential agree well with the experimental structures across all five compositions. This agreement indicates that the MLIP captures structural features across the broader compositional range and reinforces its ability to accurately capture the structure of glassy $NaFePO_4$.

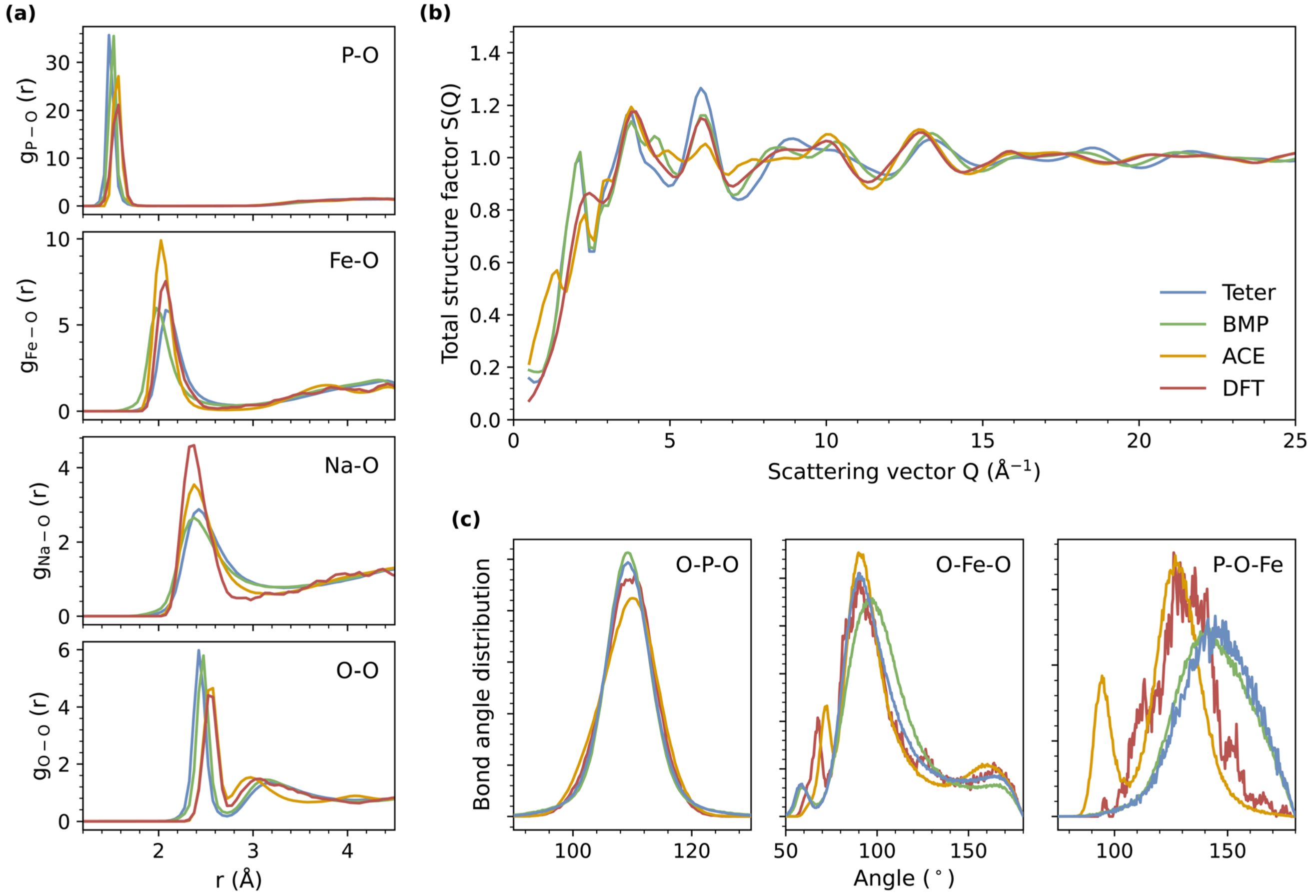

Fig. 4 Structural analysis of simulated glass structures produced with the ACE MLIP, Teter, and BMP potentials as well as AIMD based on DFT. (a) Radial distribution functions $g_{ij}(r)$ for the P–O, Fe–O, Na–O, and O–O interactions. (b) Simulated neutron total structure factor $S(Q)$. (c) Bond angle distributions for the O–P–O, O–Fe–O, and P–O–Fe angles. In all panels, results for Teter, BMP, ACE, and DFT are shown as blue, green, yellow, and red lines, respectively.

We focus our analysis of bond angle distributions on the three primary structural motifs, namely, O–P–O, O–Fe–O, and P–O–Fe (P–O–P bonds occur only in negligible quantities, see Table 1). As shown in Fig. 4C, all potentials accurately capture the inter-tetrahedral O–P–O angle, while the ACE MLIP generally provides an improved description of O–Fe–O and P–O–Fe angles compared to the classical potentials. However, the MLIP predicts an unexpected secondary peak in the P–O–Fe distribution at approximately 90°, which is attributed to edge-sharing between P tetrahedra and Fe coordination polyhedral. Notably, this is not observed in the glass structures generated using DFT.

Overall, these analyses demonstrate that the trained MLIP generates a glass structure more closely resembling DFT-derived structures compared to the classical Teter and BMP potentials. Nevertheless, the limitations in the length and time scales of DFT-based glass structures, along with the absence of experimental structure data, prevent a definitive conclusion about which potential best describes glassy $NaFePO_4$. In the following, we therefore characterize the diffusion dynamics in the system using both the MLIP and two classical potentials to provide a broader basis for comparison.

3.3 Diffusion characterization

Sampling atom dynamics of glasses and amorphous phases is not a trivial task. To describe room temperature diffusivity, the common approach is to extrapolate from high temperature diffusivity data using an Arrhenius relationship. This is because determining the high temperature diffusivity is more computationally efficient. An issue with this approach is that very high temperatures are often needed to accelerate sampling, *i.e.*, the diffusivity is often sampled at temperatures well above the glass transition temperature (T_g) or even above the melting temperature. As such, we cannot be sure that the same Arrhenius relationship connecting diffusivity and temperature applies both above and below the glass transition region. To determine the low temperature diffusivity, we have sampled the diffusivity of glass samples at six different temperatures in the range of 500–1500 K, *i.e.*, both above and below the simulated T_g of 762 to 999 K for the different potentials. We determine the diffusivity from 10 ns trajectories at the given temperature, ensuring that we reach the diffusive regime of the mean squared displacement (MSD, $\langle r_k{}^2(t)\rangle$) for Na ions for all potentials at all temperatures (Fig. 5A). MSD is calculated as,

$$r_k^2(t) = \left\langle \frac{1}{N}\sum_{j=1}^{N}\left(r_j(0) - r_j(t)\right)^2 \right\rangle \tag{7}$$

for all atoms N of a species k (k = Na, Fe, P, O) from their positions over time $r_j(t)$. The mean square displacement at each temperature for all species is shown in ESI, Fig. S4 and S5.† The diffusion coefficient for a species k, D_k, was obtained for the three potentials at different temperatures from the slope of the MSDs in the diffusive regime (>10^5 fs),

$$D_k = \frac{1}{6}\lim_{t\to\infty}\frac{d\langle r_k^2(t)\rangle}{dt} \tag{8}$$

The results for D_{Na} are shown in Fig. 5B for structures prepared in both the NVT and NPT ensembles (see Section 2.3). For all three potentials, we find that the diffusion coefficients are consistently higher in the glass structures prepared using the *NPT* compared to *NVT* ensemble. This likely arises from thermal expansion during heating, which increases the glass network volume, reducing density and thereby facilitating faster Na dynamics in NPT. A non-Arrhenius behavior in Na diffusion coefficients is evident for the Teter and BMP potentials as the systems are cooled down (beginning around 700–900 K). We have illustrated this in Fig. 5B by performing linear regression of the data above 900 K. This indicates that Na dynamics in the low-temperature glass phase exceed predictions from high-temperature extrapolations. Interestingly, the non-Arrhenius behavior is less pronounced for Na-ion diffusion in the ACE MLIP generated glass structures.

The non-Arrhenius trend observed in Fig. 5B is found in samples prepared under both NVT and NPT ensembles, suggesting that it is not driven by pressure or volumetric effects. Further analysis shows the similar non-Arrhenius behavior for all atom types across the three potentials (ESI, Fig. S6†). However, accurately determining the diffusion coefficients of Fe, P, and O atoms at low temperatures is challenging due to their limited motion, as reflected in the MSD values reported in ESI, Fig. S4 and S5.† To better understand this behavior, we relate the T_g of the simulated glasses (ESI, Fig. S7†) to the onset of the non-Arrhenius behavior in ESI, Fig. S6.† We observe that in the sampled glass systems exhibiting non-Arrhenius behavior, the deviation emerges at temperatures equal to or below the simulated glass transition temperature T_g. We note that the observed trend mirrors that seen in ionic crystals with point defects, where diffusion can be categorized into two distinct regions. Namely, a low-temperature extrinsic region, where the diffusion rate is controlled by the concentration of defects, and a high-temperature intrinsic region, where it is governed by thermally generated intrinsic defects.[60] We propose that a similar mechanism may explain the observed behavior in our glass systems, where at low temperature, the diffusion is controlled by the inherent conduction pathways in the glass structure, with the activation energy only depending on the energy of migration. As the temperature increases to above T_g, the surrounding glass network becomes mobile and thus adds an additional contribution to the activation energy.

To further characterize the Na-ion diffusion in these systems, we investigate the per-atom dynamics by calculating the self-part of the Van Hove correlation function $G_s(r,t)$,

$$G_s(r,t) = \frac{1}{N}\sum_{j=1}^{N}\delta\left(r + r_j(0) - r_j(t)\right) \tag{9}$$

which provides the probability of finding a particle j at a distance r from its original position after time t. For the sampled time of 100 ps, the function $G_s(r,t)$ for Na atoms displays a broad distribution, with probabilities extending up to, *e.g.*, 5 Å at 500 K. At elevated temperature, the distribution shifts to larger distances ($r \sim$ 1–30 Å at 1500 K) due to the increased thermal energy (Fig. 5C, ESI, Fig. S8†). From the

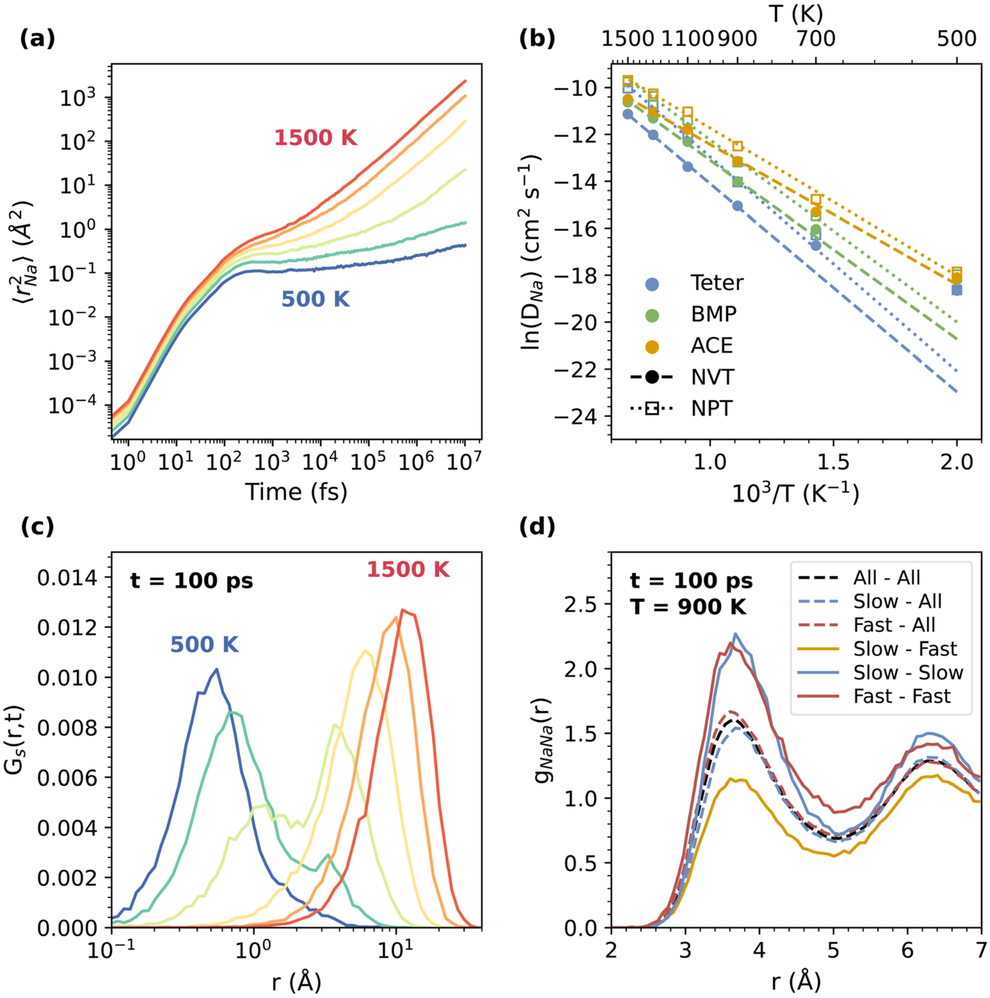

Fig. 5 (a) Mean square displacement of sodium-ion diffusion sampled in the range of 500 to 1500 K with the ACE MLIP. (b) Arrhenius plot of logarithmic diffusion coefficients as a function of inverse temperature. Lines based on linear regression of the data above 900 K are shown, visualizing ideal Arrhenius behavior (c) self part Van Hove correlation function of sodium ions after 105 fs in the range of 500–1500 K. (d) Na–Na radial distribution functions of the 25% highest (fast) and lowest (slow) mobility Na ions after 105 fs at 900 K relative to other Na ions.

MSDs seen in Fig. 5A, which is an average metric for all atoms, the Na atoms appear to move diffusively. However, as seen from the distributions of the self-part of the Van Hove correlation, the actual Na diffusion process in these glasses is influenced by significant heterogeneity. That is, a clear bimodal distribution for the Van Hove correlation function develops at 700–900 K around the glass transition of these systems, *i.e.*, at these temperatures, where the network-forming species (Fe and P) are diffusing very slowly, different atomic environments are present. In turn, this leads to very different per atom diffusive behavior.

3.4 Correlating glass structure with Na-ion dynamics

To characterize the correlation between structural features and diffusivity, we categorize the Na atoms based on their diffusivity after 100 ps at 900 K, designating the top 25% most mobile Na ions as "fast" and the bottom 25% as "slow".[61,62] The partial radial distribution functions $g_{ij}(r)$ for these two groups, as well as their interactions with all Na atoms, are presented in Fig. 5D. Additional $g_{ij}(r)$ functions depicting these mobility-labeled Na interactions with other atomic species for each potential are provided in ESI, Fig. S9 and S10.† Our analysis reveals distinct differences in the structural environments surrounding fast and slow Na atoms. That is, fast Na atoms are preferentially located near other fast Na atoms, while slow Na atoms exhibit the same clustering behavior with their counterparts. This trend is consistent across all tested potentials and simulation conditions, although the extent of clustering depends on the specific potential used. Notably, the Teter potential shows a stronger degree of fast–fast clustering, whereas the ACE MLIP exhibits a higher degree of slow–slow clustering.

Fig. 5D also reveals that fast Na atoms are surrounded by slightly more Na neighbors on average, while slow Na atoms have slightly fewer Na neighbors. This trend is observed for all potentials, but to a higher degree for the Teter and BMP potentials (ESI, Fig. S11†), where the disparity in the local Na–Na environment between fast and slow Na atoms is more pronounced than in the ACE-based potential. Furthermore, differences in the local Na–P and Na–Fe environments of fast and slow Na ions are also apparent as seen in ESI, Fig. S9 and S10,† where fast Na atoms tend to have fewer Fe and P neighbors, while slow Na atoms have comparatively more. These findings align with previous work on Na-ion dynamics in sodium containing glasses,[61,62] *i.e.*, similar tendencies for Na atoms with comparable mobility to cluster and for fast Na atoms to have fewer neighboring glass-former atoms were observed.

Fig. 6 shows a visual representation of the Na-ion diffusion trajectories. We find that some of the Na ions in the glass network are trapped in local environments that they cannot escape from during the diffusion process. This is because they are constrained by the surrounding iron and phosphate groups, leading to a low mobility during the simulated trajectory. Other Na ions are located in channel-like local environments where they can more freely diffuse.

To further characterize the effects of the local environment on the Na-ion dynamics, we next consider the effect of larger ring-type structures. In this analysis, Fe and P atoms are treated as the backbone of the glass structures, with ring structures being identified based on the network created by their bonds with O. Specifically, we compute Guttman rings,[63] defined as the shortest paths between two atoms connected by an edge, excluding the direct path. These shortest paths are calculated using Dijkstra's algorithm. The distribution of Gutmann rings in the $NaFePO_4$ glass structure from the ACE potential is shown in ESI, Fig. S12.† For each ring, we determine its center (C_{ring}) by averaging the positions of the constituent atoms. Using these centers, radial distribution functions (Fig. 7) are calculated for rings of different sizes (<6 oxygen atoms, 6–7 oxygen atoms, >7 oxygen atoms) with respect to the different categories of Na atoms (fast, slow, all). As such, Fig. 7 shows how likely it is to find Na atoms at a given distance from the center of rings, normalized based on the number of Na ions and rings of a given size.

For ring sizes below 6 (*i.e.*, less than 12 atoms in the ring), we find that the Na atoms are consistently located more than 2 Å away from the ring centers. This suggests that such rings are too small to allow Na diffusion through their center. For rings with a size of 6 or larger, Na atoms are found near the ring centers, indicating that these rings are large enough to accommodate Na-ions during diffusion. A comparison of the Na categories (fast, slow, all) shows distinct trends, namely, slow Na ions are more frequently found close to rings with sizes of 6–7, whereas fast Na ions are slightly more preferentially found near rings with a size larger than 7. This indicates that slow Na ions are situated in environments dominated by smaller, less permeable rings, which hinder their dynamics. In contrast, fast Na ions are found in regions with larger rings, which enhance their mobility and diffusivity.

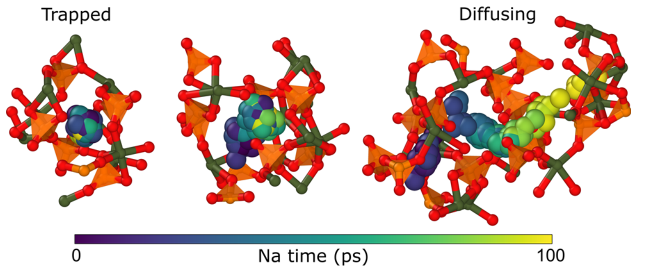

Fig. 6 Visualization of three trajectories of a single Na ion based on 100 ps diffusion at 900 K with the ACE MLIP for one glass structure. Other non-Na ions within a 4.5 Å radius of the diffusing Na ion are shown based on their initial position to illustrate the local environment. Sodium atoms are colored from blue to yellow according to the diffusion time. Na ions with the lowest (left), median (middle), and highest (right) displacement after 100 ps are shown for the given glass structure.

3.5 Perspectives

The proposed framework for parameterizing MLIPs for glass materials provides a generalizable approach to address the challenges associated with MLIPs for these materials. Our framework is system-agnostic and can be easily applied to other glass systems. The applied ACE implementation uses a relatively simple Finnis-Sinclair-type embedding, which trades some expressivity for computational tractability. This choice is justified by the moderate size and focused diversity of our dataset, which spans both equilibrium and far-from-equilibrium configurations of the $NaFePO_4$ system under varying thermal conditions. While recent equivariant universal graph neural network based MLIP architectures, such as MACE-MPA-0,[30] SevenNet-MF-ompa,[64] and Grace-1L/2L-OMAT,[65] show promise in universal accuracy and robustness, their substantially higher computational costs currently render them impractical for simulations at the scale performed herein. As such, we find that ACE offers a favorable balance between accuracy and computational efficiency, making it well-suited for the types of simulations conducted in this study.[66] However, a known limitation of local descriptor-based MLIPs, including ACE, is their poor computational scaling when multiple atom types are introduced. This arises from the combinatorial explosion of interactions, restricting their practical use to systems with approximately five or fewer atom types. Notably, recent advancements using methods such as tensor decomposition have shown promise in overcoming this limitation, enabling the development of more general local MLIPs.[65,67] Future work should explore these approaches to enhance the applicability of ACE-based potentials to more complex systems.

Additionally, it would be valuable to investigate how the $NaFePO_4$ glass structure and sodium-ion dynamics change during simulated charging and discharging. However, currently both the ACE MLIP and classical potentials face limitations in this regard. First, the ACE-based potential is currently only parameterized to account for Fe^{2+} ions in its training data, hence limiting its accuracy in describing Fe^{3+} ions, which are expected to form when transitioning from amorphous $NaFePO_4$ to $FePO_4$ during charging. Second, while the classical potentials do include parameters for Fe^{3+}, they are limited by having the oxidation state being a per atom choice. During a despoliation process, it is non-obvious which Fe atoms will switch oxidation state in the glass structure. To enable these simulations, other

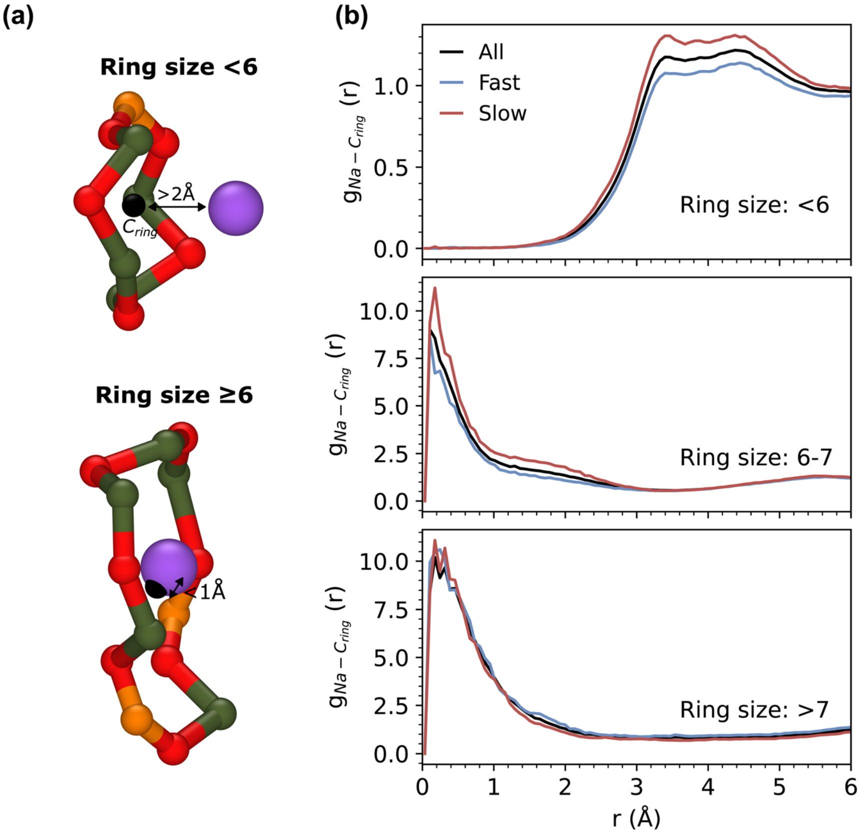

Fig. 7 (a) Visualization of how close Na ions are to relatively small (top) and large (bottom) Gutmann rings. The black sphere indicates the center of the ring (C_{ring}). (b) Radial distribution functions $g(r)$ of the of C_{ring} of rings of different sizes (<6, 6–7, >7) to the 25% highest (fast) and lowest (slow) mobility Na ions after 105 fs at 900 K.

potential architectures that can handle variable charges, such as reactive forcefields or alternative machine learning forcefields,[68–70] would be interesting to explore.

4. Conclusions

In this study, we have investigated the Na-ion dynamics of a glassy electrode material, $NaFePO_4$, as a potential low-cost material for sodium-ion batteries. To this end, we have developed a parameterization workflow using ACE and active learning tailored for disordered materials. Our MLIP developed for $NaFePO_4$ has been rigorously validated against DFT calculations, demonstrating excellent agreement in energy and force predictions. Using this potential, we have generated melt-quenched $NaFePO_4$ glass structures and accurately reproduced structural properties as compared to DFT results.

The MLIP has been used to explore Na-ion diffusion over a temperature range of 500 to 1500 K, observing significant self-diffusion of Na ions, consistent with prior experimental findings. Analysis of diffusion trajectories has revealed heterogeneous diffusion, where some Na ions diffuse extensively, while others remain localized. We have linked this behavior to differences in local environments, with fast-diffusing Na ions showing clustering and exhibiting more Na neighbors but fewer Fe and P neighbors compared to the slower Na ions. Notably, slow Na ions are predominantly located near small ring structures. These results indicate that the disorder-induced conduction, occurring with the transition from the maricite crystal to amorphous $NaFePO_4$, is linked to the formation of less constrained atomic environments for sodium, facilitating faster ionic conduction.

Overall, the trained MLIP has demonstrated robust performance in capturing the complex dynamics of an amorphous system, thus validating our proposed workflow as a powerful tool for investigating amorphous materials. Future work could expand the workflow to include multicomponent systems with diverse elements, thereby enhancing the universality of MLIPs for amorphous materials. These advancements thus hold promise for accelerating the design and optimization of next-generation materials for energy storage and other technological applications.

Data availability

The final training dataset containing atomic structures and corresponding energies and forces, as well as the parameterized ACE-based potential, are publicly available on GitHub (**https://github.com/R-Chr/NaFePO4_potential**). The workflow implementations, along with documentation on the use of the workflow, can also be found on GitHub (**https://github.com/R-**

Chr/vitrum/). Other data supporting the results within this paper are available from the corresponding author upon request.

Author contributions

R. C. and M. M. S. conceived the study and planned computational work. R. C. performed the computational work and developed all code. All authors participated in discussing the data. R. C. wrote the manuscript with revisions from M. M. S and K. A. P. M. M. S. and K. A. P. supervised the project.

Conflicts of interest

The authors declare that they have no known competing financial interests or personal relationships that could have appeared to influence the work reported in this paper.

Acknowledgements

This work was supported by the Danish Data Science Academy, which in turn is funded by the Novo Nordisk Foundation (NNF21SA0069429) and VILLUM FONDEN (40516). K.P. was supported by the Energy Storage Research Alliance ''ESRA'' (DE-AC02-06CH11357), an Energy Innovation Hub funded by the US Department of Energy, Office of Science, Basic Energy Sciences. We acknowledge the computational resources provided from Aalborg University for through CLAAUDIA, the National Energy Research Scientific Computing Center (NERSC), a facility of the U.S. Department of Energy Office of Science at Lawrence Berkeley National Laboratory (DE-AC02-05-CH11231), and EuroHPC Joint Undertaking with access to Vega at IZUM, Slovenia (EHPC-REG-2022R02-224).

References

1 J.-M. Tarascon and M. Armand, Issues and challenges facing rechargeable lithium batteries, *Nature*, 2001, **414**, 359–367.
2 M. Armand and J.-M. Tarascon, Building better batteries, *Nature*, 2008, **451**, 652–657.
3 Z. Yang, J. Zhang, M. C. W. Kintner-Meyer, X. Lu, D. Choi, J. P. Lemmon and J. Liu, Electrochemical energy storage for green grid, *Chem. Rev.*, 2011, **111**, 3577–3613.
4 K. Chayambuka, G. Mulder, D. L. Danilov and P. H. L. Notten, From Li-ion batteries toward Na-ion chemistries: challenges and opportunities, *Adv. Energy Mater.*, 2020, **10**, 2001310.
5 N. Muralidharan, E. C. Self, M. Dixit, Z. Du, R. Essehli, R. Amin, J. Nanda and I. Belharouak, Next-generation cobalt-free cathodes – A prospective solution to the battery industry's cobalt problem, *Adv. Energy Mater.*, 2022, **12**, 2103050.
6 M. He, S. Liu, J. Wu and J. Zhu, Review of cathode materials for sodium-ion batteries, *Prog. Solid State Chem.*, 2024, **74**, 100452.
7 H. Pan, Y.-S. Hu and L. Chen, Room-temperature stationary sodium-ion batteries for large-scale electric energy storage, *Energy Environ. Sci.*, 2013, **6**, 2338–2360.
8 X. Ma, H. Chen and G. Ceder, Electrochemical properties of monoclinic $NaMnO_2$, *J. Electrochem. Soc.*, 2011, **158**, A1307.
9 H. Su, S. Jaffer and H. Yu, Transition metal oxides for sodium-ion batteries, *Energy Storage Mater.*, 2016, **5**, 116–131.
10 C. Masquelier and L. Croguennec, Polyanionic (phosphates, silicates, sulfates) frameworks as electrode materials for rechargeable Li (or Na) batteries, *Chem. Rev.*, 2013, **113**, 6552–6591.
11 H. Liao, Z. Zhang, Y. Zheng and Y. Gao, $NaFePO_4$ for sodium-ion batteries: mechanism, synthesis and optimization strategies toward commercialization, *Energy Storage Mater.*, 2024, **65**, 103157.
12 A. K. Padhi, K. S. Nanjundaswamy and J. B. Goodenough, Phospho-olivines as positive-electrode materials for rechargeable lithium batteries, *J. Electrochem. Soc.*, 1997, **144**, 1188.
13 R. Kapaev, A. Chekannikov, S. Novikova, S. Yaroslavtsev, T. Kulova, V. Rusakov, A. Skundin and A. Yaroslavtsev, Mechanochemical treatment of maricite-type $NaFePO_4$ for achieving high electrochemical performance, *J. Solid State Electrochem.*, 2017, **21**, 2373–2380.
14 F. Xiong, Q. An, L. Xia, Y. Zhao, L. Mai, H. Tao and Y. Yue, Revealing the atomistic origin of the disorder-enhanced Na-storage performance in $NaFePO_4$ battery cathode, *Nano Energy*, 2019, **57**, 608–615.
15 G. Ali, J.-H. Lee, D. Susanto, S.-W. Choi, B. W. Cho, K.-W. Nam and K. Y. Chung, Polythiophene-wrapped olivine $NaFePO_4$ as a cathode for Na-ion batteries, *ACS Appl. Mater. Interfaces*, 2016, **8**, 15422–15429.
16 J. Kim, D.-H. Seo, H. Kim, I. Park, J.-K. Yoo, S.-K. Jung, Y.-U. Park, W. A. Goddard III and K. Kang, Unexpected discovery of low-cost maricite $NaFePO_4$ as a high-performance electrode for Na-ion batteries, *Energy Environ. Sci.*, 2015, **8**, 540–545.
17 Y. Liu, N. Zhang, F. Wang, X. Liu, L. Jiao and L. Fan, Approaching the downsizing limit of maricite $NaFePO_4$ toward high-performance cathode for sodium-ion batteries, *Adv. Funct. Mater.*, 2018, **28**, 1801917.
18 R. R. Kapaev, S. A. Novikova, A. B. Yaroslavtsev, A. A. Chekannikov, T. L. Kulova and A. M. Skundin, Activation of $NaFePO_4$ with maricite structure for application as a cathode material in sodium-ion batteries, *Mendeleev Commun.*, 2017, **27**, 263–264.
19 S. Nakata, T. Togashi, T. Honma and T. Komatsu, Cathode properties of sodium iron phosphate glass for sodium ion batteries, *J. Non Cryst. Solids*, 2016, **450**, 109–115.
20 M. Hiratsuka, T. Honma and T. Komatsu, Vitrification of maricite $NaFePO_4$ crystal by laser irradiation and enhanced sodium ion battery performance, *J. Alloys Compd.*, 2021, **885**, 160928.
21 Z. Chen, T. Du, N. M. A. Krishnan, Y. Yue and M. M. Smedskjaer, Disorder-induced enhancement of

lithium-ion transport in solid-state electrolytes, *Nat. Commun.*, 2025, **16**, 1057.

22 J. H. Bong and S. Adams, Molecular dynamics simulations of amorphous $NaFePO_4$ as an Na-ion battery cathode material, *Funct. Mater. Lett.*, 2021, **14**, 2141006.

23 J. Du and A. N. Cormack, The medium range structure of sodium silicate glasses: a molecular dynamics simulation, *J. Non Cryst Solids*, 2004, **349**, 66–79.

24 P. Goj and P. Stoch, Molecular dynamics simulations of P_2O_5-Fe_2O_3-FeO-Na_2O glasses, *J. Non Cryst. Solids*, 2018, **500**, 70–77.

25 B. Al-Hasni and G. Mountjoy, Structural investigation of iron phosphate glasses using molecular dynamics simulation, *J. Non Cryst. Solids*, 2011, **357**, 2775–2779.

26 K. Joseph, K. Jolley and R. Smith, Iron phosphate glasses: structure determination and displacement energy thresholds, using a fixed charge potential model, *J. Non Cryst. Solids*, 2015, **411**, 137–144.

27 G. Malavasi and A. Pedone, The effect of the incorporation of catalase mimetic activity cations on the structural, thermal and chemical durability properties of the 45S5 Bioglass®, *Acta Mater.*, 2022, **229**, 117801.

28 M. Bertani, M. C. Menziani and A. Pedone, Improved empirical force field for multicomponent oxide glasses and crystals, *Phys. Rev. Mater.*, 2021, **5**, 45602.

29 B. Deng, P. Zhong, K. Jun, J. Riebesell, K. Han, C. J. Bartel and G. Ceder, CHGNet as a pretrained universal neural network potential for charge-informed atomistic modelling, *Nat. Mach Intell.*, 2023, **5**, 1031–1041.

30 I. Batatia, *et al.*, A foundation model for atomistic materials chemistry, *arxiv*, 2024, preprint, arXiv:2401.00096, DOI: **10.48550/arXiv.2401.00096**.

31 B. Deng, Y. Choi, P. Zhong, J. Riebesell, S. Anand, Z. Li, K. Jun, K. A. Persson and G. Ceder, Systematic softening in universal machine learning interatomic potentials, *NPJ Comput. Mater.*, 2025, **11**, 9.

32 H. Zheng, E. Sivonxay, R. Christensen, M. Gallant, Z. Luo, M. McDermott, P. Huck, M. M. Smedskjær and K. A. Persson, The *ab initio* non-crystalline structure database: empowering machine learning to decode diffusivity, *NPJ Comput. Mater.*, 2024, **10**, 295.

33 R. Drautz, Atomic cluster expansion for accurate and transferable interatomic potentials, *Phys. Rev. B*, 2019, **99**, 14104.

34 Y. Lysogorskiy, C. van der Oord, A. Bochkarev, S. Menon, M. Rinaldi, T. Hammerschmidt, M. Mrovec, A. Thompson, G. Csányi, C. Ortner and R. Drautz, Performant implementation of the atomic cluster expansion (PACE) and application to copper and silicon, *NPJ Comput. Mater.*, 2021, **7**, 97.

35 V. Bihani, S. Mannan, U. Pratiush, T. Du, Z. Chen, S. Miret, M. Micoulaut, M. M. Smedskjaer, S. Ranu and N. M. A. Krishnan, EGraFFBench: evaluation of equivariant graph neural network force fields for atomistic simulations, *Digital Discovery*, 2024, **3**, 759–768.

36 A. M. Tokita and J. Behler, How to train a neural network potential, *J. Chem. Phys.*, 2023, **159**, 121501.

37 Y. Lysogorskiy, A. Bochkarev, M. Mrovec and R. Drautz, Active learning strategies for atomic cluster expansion models, *Phys. Rev. Mater.*, 2023, **7**, 43801.

38 G. Kresse and J. Hafner, *Ab initio* molecular dynamics for liquid metals, *Phys. Rev. B: Condens. Matter Mater. Phys.*, 1993, **47**, 558–561.

39 G. Kresse and J. Furthmüller, Efficiency of *ab initio* total energy calculations for metals and semiconductors using a plane-wave basis set, *Comput. Mater. Sci.*, 1996, **6**, 15–50.

40 G. Kresse and J. Furthmüller, Efficient iterative schemes for *ab initio* total-energy calculations using a plane-wave basis set, *Phys. Rev. B: Condens. Matter Mater. Phys.*, 1996, **54**, 11169–11186.

41 P. E. Blöchl, Projector augmented-wave method, *Phys. Rev. B: Condens. Matter Mater. Phys.*, 1994, **50**, 17953.

42 J. P. Perdew, K. Burke and M. Ernzerhof, Generalized gradient approximation made simple, *Phys. Rev. Lett.*, 1996, **77**, 3865.

43 A. Jain, S. P. Ong, G. Hautier, W. Chen, W. D. Richards, S. Dacek, S. Cholia, D. Gunter, D. Skinner and G. Ceder, Commentary: the materials project: a materials genome approach to accelerating materials innovation, *APL Mater.*, 2013, **1**, 011002.

44 A. P. Thompson, H. M. Aktulga, R. Berger, D. S. Bolintineanu, W. M. Brown, P. S. Crozier, P. J. in 't Veld, A. Kohlmeyer, S. G. Moore, T. D. Nguyen, R. Shan, M. J. Stevens, J. Tranchida, C. Trott and S. J. Plimpton, LAMMPS – a flexible simulation tool for particle-based materials modeling at the atomic, meso, and continuum scales, *Comput. Phys. Commun.*, 2022, **271**, 108171.

45 A. Hjorth Larsen, et al., The atomic simulation environment—a python library for working with atoms, *J. Phys.: Condens. Matter*, 2017, **29**, 273002.

46 S. P. Ong, W. D. Richards, A. Jain, G. Hautier, M. Kocher, S. Cholia, D. Gunter, V. L. Chevrier, K. A. Persson and G. Ceder, Python materials genomics (pymatgen): a robust, open-source python library for materials analysis, *Comput. Mater. Sci.*, 2013, **68**, 314–319.

47 A. Ganose, J. Riebesell, J. George, J. X. Shen, A. S. Rosen, A. A. Naik, N. Winner, M. Wen, R. Guha and M. Kuner, *atomate2*, 2024. **https://github.com/materialsproject/atomate2**.

48 A. S. Rosen, M. Gallant, J. George, J. Riebesell, H. Sahasrabuddhe, J.-X. Shen, M. Wen, M. L. Evans, G. Petretto, D. Waroquiers, G.-M. Rignanese, K. A. Persson, A. Jain and A. M. J. Ganose, Computational workflows made simple, *J. Open Source Softw.*, 2024, **9**, 5995.

49 A. Jain, S. P. Ong, W. Chen, B. Medasani, X. Qu, M. Kocher, M. Brafman, G. Petretto, G.-M. Rignanese, G. Hautier, D. Gunter and K. A. Persson, FireWorks: a dynamic workflow system designed for high-throughput applications, *Concurr. Comput.*, 2015, **27**, 5037–5059.

50 A. Bochkarev, Y. Lysogorskiy, S. Menon, M. Qamar, M. Mrovec and R. Drautz, Efficient parametrization of the atomic cluster expansion, *Phys. Rev. Mater.*, 2022, **6**, 13804.

51 L. C. Erhard, J. Rohrer, K. Albe and V. L. Deringer, Modelling atomic and nanoscale structure in the silicon–oxygen system

through active machine learning, *Nat. Commun.*, 2024, **15**, 1927.

52 L. Kahle and F. Zipoli, Quality of uncertainty estimates from neural network potential ensembles, *Phys. Rev. E*, 2022, **105**, 15311.

53 J. S. Smith, B. Nebgen, N. Lubbers, O. Isayev and A. E. Roitberg, Less is more: Sampling chemical space with active learning, *J. Chem. Phys.*, 2018, **148**, 241733.

54 A. P. Bartók and G. Csányi, Gaussian approximation potentials: a brief tutorial introduction, *Int. J. Quantum Chem.*, 2015, **115**, 1051–1057.

55 J. Vandermause, S. B. Torrisi, S. Batzner, Y. Xie, L. Sun, A. M. Kolpak and B. Kozinsky, On-the-fly active learning of interpretable Bayesian force fields for atomistic rare events, *NPJ Comput. Mater.*, 2020, **6**, 20.

56 E. V. Podryabinkin, E. V. Tikhonov, A. V. Shapeev and A. R. Oganov, Accelerating crystal structure prediction by machine-learning interatomic potentials with active learning, *Phys. Rev. B*, 2019, **99**, 64114.

57 E. V. Podryabinkin and A. V. Shapeev, Active learning of linearly parametrized interatomic potentials, *Comput. Mater. Sci.*, 2017, **140**, 171–180.

58 M. Bertani, T. Charpentier, F. Faglioni and A. Pedone, Accurate and transferable machine learning potential for molecular dynamics simulation of sodium silicate glasses, *J. Chem. Theory Comput.*, 2024, **20**, 1358–1370.

59 D. Tunega, T. Bučko and A. Zaoui, Assessment of ten DFT methods in predicting structures of sheet silicates: Importance of dispersion corrections, *J. Chem. Phys.*, 2012, **137**, 114105.

60 K. Funke, Solid state ionics: from michael faraday to green energy—the European dimension, *Sci. Technol. Adv. Mater.*, 2013, **14**, 043502.

61 R. Christensen and M. M. Smedskjaer, Predicting dynamics from structure in a sodium silicate glass, *MRS Bull.*, 2025, **50**, 236–246.

62 S. S. Sørensen, M. M. Smedskjaer and M. Micoulaut, Evidence for complex dynamics in glassy fast ion conductors: the case of sodium thiosilicates, *J. Phys. Chem. B*, 2023, **127**, 10179–10188.

63 L. Guttman, Ring structure of the crystalline and amorphous forms of silicon dioxide, *J. Non-Cryst. Solids*, 1990, **116**, 145–147.

64 J. Kim, J. Kim, J. Kim, J. Lee, Y. Park, Y. Kang and S. Han, Data-efficient multifidelity training for high-fidelity machine learning interatomic potentials, *J. Am. Chem. Soc.*, 2025, **147**, 1042–1054.

65 A. Bochkarev, Y. Lysogorskiy and R. Drautz, Graph atomic cluster expansion for semilocal interactions beyond equivariant message passing, *Phys. Rev. X*, 2024, **14**, 21036.

66 T. W. Ko and S. P. Ong, Recent advances and outstanding challenges for machine learning interatomic potentials, *Nat. Comput. Sci.*, 2023, **3**, 998–1000.

67 J. P. Darby, D. P. Kovács, I. Batatia, M. A. Caro, G. L. W. Hart, C. Ortner and G. Csányi, Tensor-reduced atomic density representations, *Phys. Rev. Lett.*, 2023, **131**, 28001.

68 T. P. Senftle, S. Hong, M. M. Islam, S. B. Kylasa, Y. Zheng, Y. K. Shin, C. Junkermeier, R. Engel-Herbert, M. J. Janik, H. M. Aktulga, T. Verstraelen, A. Grama and A. C. T. van Duin, The ReaxFF reactive force-field: development, applications and future directions, *NPJ Comput. Mater.*, 2016, **2**, 15011.

69 M. Rinaldi, M. Mrovec, A. Bochkarev, Y. Lysogorskiy and R. Drautz, Non-collinear magnetic atomic cluster expansion for iron, *NPJ Comput. Mater.*, 2024, **10**, 12.

70 B. Deng, P. Zhong, K. Jun, J. Riebesell, K. Han, C. J. Bartel and G. Ceder, CHGNet as a pretrained universal neural network potential for charge-informed atomistic modelling, *Nat. Mach. Intell.*, 2023, **5**, 1031–1041.